Effect of Background Pressure on the Performance and Plume of the HiVHAc Hall Thruster

IEPC-2013-058

Presented at the 33rd International Electric Propulsion Conference,
The George Washington University • Washington, D.C. • USA
October 6 – 10, 2013

Wensheng Huang*, Hani Kamhawi†, and Thomas Haag‡
National Aeronautics and Space Administration Glenn Research Center, Cleveland, Ohio, 44135, USA

During the Single String Integration Test of the NASA HiVHAc Hall thruster, a number of plasma diagnostics were implemented to study the effect of varying facility background pressure on thruster operation. These diagnostics include thrust stand, Faraday probe, ExB probe, and retarding potential analyzer. The test results indicated a rise in thrust and discharge current with background pressure. There was also a decrease in ion energy per charge, an increase in multiply-charged species production, a decrease in plume divergence, and a decrease in ion beam current with increasing background pressure. A simplified ingestion model was applied to determine the maximum acceptable background pressure for thrust measurement. The maximum acceptable ingestion percentage was found to be around 1%. Examination of the diagnostics results suggest the ionization and acceleration zones of the thruster were shifting upstream with increasing background pressure.

Abbreviations and Nomenclature

GRC = Glenn Research Center
SMD = Science Mission Directorate
ISPT = In-Space Propulsion Technology
HiVHAc = High Voltage Hall Accelerator
EDU = Engineering Development Unit
RPA = Retarding Potential Analyzer
CEX = Charge-exchange
SEE = Secondary Electron Emission
MCD = Mean Channel Diameter
η_a = Anode efficiency
η_v = Voltage utilization efficiency
η_d = Divergence efficiency
η_b = Current utilization efficiency
η_m = Mass utilization efficiency
η_q = Charge utilization efficiency

I. Introduction

THE, development of the NASA High Voltage Hall Accelerator (HiVHAc) Hall thruster continues to progress steadily. This project is funded by the NASA Science Mission Directorate's (SMD's) In-Space Propulsion Technology (ISPT) program to deliver a Hall thruster beyond the current state-of-the-art (SOTA) that is capable of enabling various Discovery class missions. Mission studies in 2009 showed that the 3.5-kW HiVHAc is able to outperform an SotA 4.5-kW flight Hall thruster by delivering 6-12% more mass on four missions of interest.[1] These missions include Vesta-Ceres rendezvous (the Dawn mission), Koppf comet rendezvous, Nereus (a near-Earth asteroid) sample return, and NEARER, which involves two near-Earth asteroid returns. The thrust profiles of the missions range from ones that favor high specific impulse to ones that favor high thrust-to-power demonstrating the wide throttle-ability of the 3.5-kW HiVHAc.

* Research Engineer, Propulsion and Propellants, wensheng.huang@nasa.gov.
† Research Engineer, Propulsion and Propellants, hani.kamhawi-1@nasa.gov.
‡ Propulsion Engineer, Space Propulsion, thomas.w.haag@nasa.gov.

The current iteration of the HiVHAc Hall thruster is the Engineering Development Unit 2 (EDU2). This version of the HiVHAc features a discharge channel replacement mechanism designed to guarantee long operational life time for high specific impulse (high discharge voltage) operation. Compared to the previous iteration, which is the EDU1, the EDU2 has better thermal management, simpler design for the channel replacement mechanism, and superior voltage isolation. The EDU2 has undergone the performance acceptance test (PAT),[2] a vibration test,[2] a plume divergence characterization tests,[3] an in-situ mechanism actuation tests (unpublished), and a single-string integration test (SSIT).[4] Further testing will likely involve some form of wear test, which is very resource intensive. The team decided to determine the minimum requirements on the facility for high-fidelity testing. The HiVHAc development team decided to perform a series of tests together with the SSIT to better characterize the behavior of the HiVHAc thruster in a space-like environment.

To reach an environment as close to space-like as possible, the EDU2 was tested in NASA Glenn Research Center's (GRC's) Vacuum Facility 5 (VF5). Many diagnostics were instrumented as a part of the testing, including a thrust stand, a retarding potential analyzer (RPA), a Wien filter, also known as ExB probe, a Faraday probe, an infrared camera, a high-speed camera, and a set of high-speed Langmuir probes. Details regarding the SSIT test setup can be found in Kamhawi's papers.[4] The present paper will focus on the diagnostics typically used for characterizing performance-driving physics, specifically the thrust stand, the RPA, the ExB probe, and the Faraday probe.

II. Background

This study is an attempt to determine how the physics of the HiVHAc EDU2 changes with background facility pressure. The performance of a Hall thruster can be measured by its anode efficiency, defined in Eq. (1).

$$\eta_a = \frac{T^2}{2\dot{m}_a I_d V_d} \tag{1}$$

In this equation, T is thrust, $\dot{m}_a$ is anode mass flow rate, I_d is discharge current, and V_d is discharge voltage. However, the anode efficiency alone does not provide information about the plasma generation and acceleration processes that drive the performance of the thruster.

A phenomenological efficiency model is a method of breaking down and describing various physical phenomena that affect the overall efficiency of a Hall thruster. The purpose of a phenomenological efficiency model is to help researchers quantify the trends in the processes that drive the overall thruster efficiency. Many efficiency models have been proposed for the Hall thruster in the past. The complexity of these models depended on the operating environment and the state of knowledge in the community at the time. The model used in this paper is the same as a prior work by Shastry,[5] which has evolved over time from a number of other studies.[6-9] The model is shown in Eq. (2) to (7).

$$\eta_a = \eta_v \eta_d \eta_b \eta_m \eta_q \tag{2}$$

$$\eta_v = \frac{V_{RPA}}{V_d} \tag{3}$$

$$\eta_d = (\cos\ \delta)^2 \tag{4}$$

$$\eta_b = \frac{I_b}{I_d} \tag{5}$$

$$\eta_m = \left(\frac{m_{Xe} I_b}{\dot{m}_a e}\right)\alpha_m, \quad \alpha_m = \sum_k \frac{\Omega_k}{Z_k} \tag{6}$$

$$\eta_q = \frac{\left(\sum_k \Omega_k / \sqrt{Z_k}\right)^2}{\sum_k \Omega_k / Z_k} \tag{7}$$

Where η_a, the anode efficiency, is the same as that calculated from Eq. (1), η_v is the voltage utilization efficiency, η_d is the divergence efficiency, η_b is current utilization efficiency, η_m is the mass utilization efficiency, η_q is the charge utilization efficiency, V_{RPA} is the average ion energy per charge, δ is the charged-weighted divergence angle, the I_b is the total beam current, m_{Xe} is the mass of a xenon atom, e is the elementary charge constant, α_m is the part of mass utilization efficiency that depends on charge state information, Ω_k is the current fraction of the k-th species, and Z_k is the charge of the k-th species.

The voltage utilization efficiency describes, on the average, how much of the voltage provided by the discharge supply is actually used to accelerate the ions. This factor is typically measured by the RPA.

The divergence efficiency describes how much of the kinetic energy imparted to the ions is axial, thrust-producing, kinetic energy. This factor is typically measured by the Faraday probe.

The current utilization efficiency describes how much of the discharge current is carried by ions instead of electrons. Electrons generate negligible thrust compared to the ions. This factor is typically measured by the Faraday probe.

The mass utilization efficiency describes how much of the mass flow exiting the thruster channel is in the form of ions. This factor typically requires data from the Faraday probe and the ExB probe.

The charge utilization efficiency is a number of terms representing the effects of having multiply-charged species that are not already described by the other terms in the efficiency model.

III. Experimental Setup

To simplify plot labeling, throttle point notation from the SSIT will be used. Operating conditions are labeled as vvv-k.k-Pnx, where vvv is the discharge voltage in volts, k.k is the discharge power in kilowatts, and n is the normalized background pressure, defined as the number of multiples of the lowest achievable operating background pressure for the throttle point vvv-k.k. This pressure is measured by an ion gauge located right below the thrust stand. For example P1x indicates the operating condition corresponding to the minimum achieved background pressure, while P10x indicates the background pressure is ten times that of P1x. Unless otherwise noted, all spatial positions presented in this paper have been normalized by the mean channel diameter (MCD) of the thruster. MCD is defined as the average of the inner and outer discharge-channel wall diameters.

A. Thrusters and Test Matrix

The NASA HiVHAc EDU2 is a 3.9-kW xenon Hall thruster. The thruster is highly throttle-able. The discharge voltage can vary from 200 to 650 V, corresponding to specific impulse values of 1200 to 2700 s. The discharge power ranges from 0.3 to 3.9 kW. During testing, the magnetic field settings are selected to create a magnetic lens symmetric about the channel centerline, while maximizing total efficiency. This magnetic field setting optimization is performed at the lowest achievable background pressure for each throttle point. Figure 1 shows a picture of the NASA HiVHAc EDU2 with various test equipment.

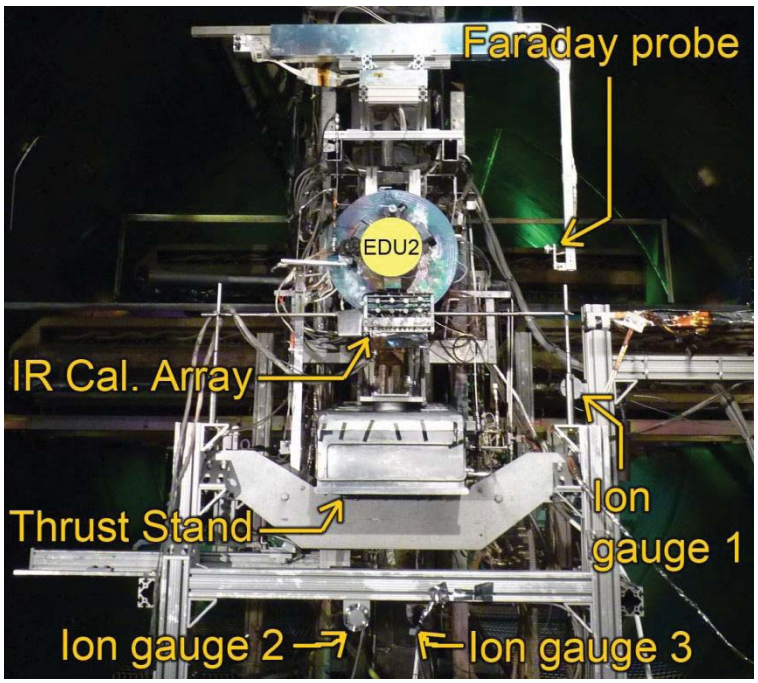

Figure 1. NASA HiVHAc EDU2 and thrust stand setup.

For the purpose of this test, seven throttling points were selected. These seven points are 300-1.5, 300-3.0, 400-2.0, 400-3.2, 500-2.0, 500-3.0, and 500-3.9. At each throttling point, the thruster settings are optimized at the lowest achievable pressure as measured by the ion gauges next to the thrust stand. Then, the background pressure was raised by injecting xenon via an auxiliary flow line that exits at >4 meters downstream of the thruster pointed away from the thruster.

B. Test Facility

Testing was conducted in NASA GRC's VF5. This cylindrical facility is 4.6 m in diameter, 18.3 m long, and is pumped with a set of cryo-panels and 20 oil diffusion pumps. The thruster was mounted on a thrust stand located close to the cryo-panels, with the thruster firing away from the panels. Facility pressures were monitored with four ion gauges, three of which were mounted next to the thrust stand and the fourth being on the facility wall axially close to the thruster. Manufacturer specifications state that the ion gauges are accurate to ±6% of reading. The positions of the gauges are shown in Fig. 1. Ion gauges 1 and 2 are both facing downstream while ion gauge 3 is facing upstream. Ion gauge 1 and 2 agree to within 10% of each other. Ion gauge 3 reports 0.63 to 0.72 times the reading as ion gauge 2. Ion gauge 2 readings were used to determine the number of multiples of the lowest achievable background pressure that the thruster was experiencing. The lowest pressure achieved for each tested condition, corrected for xenon, varied from 1.4×10^{-6} to 2.2×10^{-6} Torr.

Thruster propellant was supplied via commercially available mass flow controllers. These mass flow controllers were calibrated using xenon prior to testing. Typical uncertainty of measurement was ±1.0% of reading. Research-grade xenon was used.

Thruster electrical power was supplied via the Colorado Power Electronics (CPE) brassboard #2 (BB#2) power processing unit (PPU).[10] This PPU is capable of supplying 200 to 700 V at up to 4 kW over the main discharge line as well as supply power to the cathode heater, keeper, and magnet electrical circuits. The PPU was located outside of the vacuum facility during testing.

C. Thrust Stand and Plasma Diagnostics

This section will describe the thrust stand and the plasma diagnostics used to obtain data for the efficiency model. The plasma probes used in this study included a Langmuir probe, an RPA, an ExB probe, and a Faraday probe. Unless otherwise stated, all probe biases were applied with commercial power supplies.

The thrust stand used in this study is an inverted pendulum thrust stand designed by Haag.[11] The thrust stand is actively cooled during operation. The nominal accuracy of this thrust stand is ±2%.[12] Long-term thermal drift is corrected by measuring the thrust signal with all gas flow to the thruster off and then assuming a linear change in the zero-thrust value over time. The maximum thermal drift was found to be ~6 mN.

Figure 2 shows a photograph of the farfield probe stand. A Langmuir probe, an RPA, and an ExB probe were mounted to this probe stand with accompanying shielding and shutters to protect the RPA and ExB probe. This probe stand is fixed at ~40 MCD downstream of the thruster. The farfield Faraday probe was mounted onto a commercially available motion system that can provide both polar and radial motion (see Fig. 1). Positioning accuracy of this motion system is <2 mm and <0.2°, respectively.

The Langmuir probe consists of a single tungsten wire protruding from an alumina tube. This probe was used to obtain the local plasma potential so that the RPA data can be corrected by this potential. The Langmuir probe was swept at 2 ramps per second for 1 second at each test point. The probe was connected to a custom circuit box where the probe current was passed through a shunt and the signal fed to an isolation amplifier. The bias voltage was passed through a voltage divider and fed to another isolation amplifier. Signals from the amplifiers were fed to a data acquisition unit.

The RPA used in this study has a four-grid design. During testing, the electron suppression and repelling grids were biased to -30 V with respect to facility ground while the ion retarding grid voltage was swept. The ion retarding grid was biased by a sourcemeter while the collected current was measured by a picoammeter.

The ExB probe is a commercial product and was used to measure charged species current fraction. This ExB probe was the result of a Small Business Innovation Research project and has a proven history of usage.[8] The ExB probe has an input collimator, a filter section, and a drift section to improve the probe resolution. The electron suppression plate was biased at -30 V with respect to facility ground to

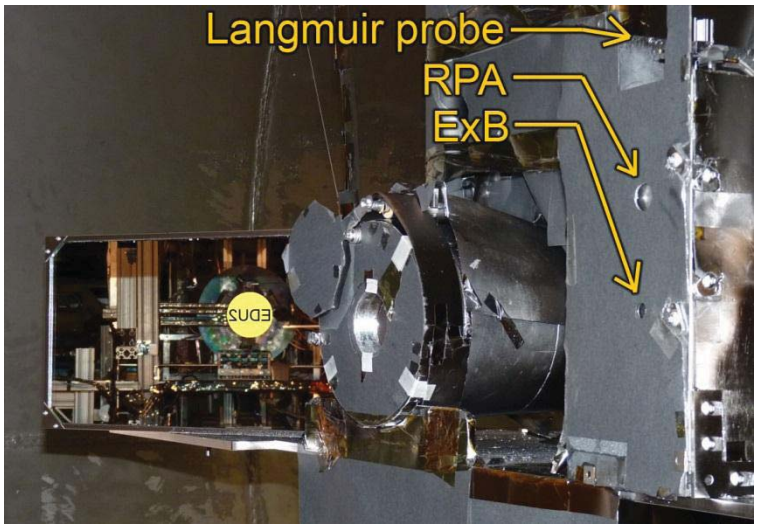

Figure 2. Photograph of the probe stand setup.

suppress secondary electron emission (SEE) from the collector. The main bias plate voltage was swept by a picoammeter, which also measured the collector current.

The Faraday probe, which is a GRC design, was used to measure ion current density in the farfield plume. Figure 3 shows a cross-sectional diagram of this Faraday probe. The collector area is a circle of diameter 17.39 mm. The front area of the collector is 238 mm^2. The probe has an overall diameter of ~28 mm. The collector and guard ring are made of molybdenum (to minimize SEE effect) and the insulating back is made of Macor. The collector and guard ring connections are mated to wires behind the insulating back and covered with fiberglass tape. At each operating condition, the Faraday probe was rotated around the center of the thruster exit plane at four different distances. The values of these four distances were 5, 6.7, 8.4, and 10.1 MCD. During testing, measurements were made at different bias voltages in increments of 10 V. The results indicate that -20 V bias with respect to facility ground is sufficient to repel incoming electrons for all operating conditions. Collected current was measured via a shunt and an isolation amplifier. The output of the amplifier was fed to the aforementioned data acquisition unit.

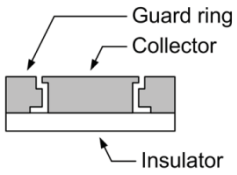

Figure 3. Non-scaled diagram of the farfield Faraday probe.

The experiment was conducted via a LabVIEW program from a dedicated data acquisition computer. The motion stages were operated by a controller that received movement commands from the computer. Encoder signals from the stages were fed into an encoder controller, which reports to the computer. The NI cDAQ-9178 data acquisition device and the various Keithley devices fed data to and were commanded by the computer. During the experiment, the computer automatically orchestrated the sequence of events that activated the various motion stages, shutters, and probes.

IV. Data Reduction

Data reduction was carried out in a specific sequence because, for the most part, each step of the analysis depended on the data obtained in the preceding steps. Though some of the analysis steps can be carried out independently, the accuracy of the result would decrease. For this study, the data analysis sequence was as follows, Langmuir probe analysis, RPA analysis, ExB probe analysis, and Faraday probe analysis. Additionally, facility pressure data is analyzed to help correct the ExB probe data for facility-background CEX effects.

A. Langmuir Probe and RPA Analysis

Langmuir probe analysis was carried out using simple Langmuir probe theory.[13] Each Langmuir probe data file contained 5000 data points. These data were ensemble averaged then smoothed using a Savitzky-Golay filter.[14, 15] Next, the derivative of the probe current with respect to the probe voltage was plotted against the probe voltage. The voltage corresponding to the highest amplitude value on this plot is roughly equal to the plasma potential. This potential is needed to correct the RPA reading because the RPA ion retarding grid was biased with respect to the facility ground. The true filter voltage was equal to the ion retarding grid bias voltage minus the local plasma potential.

RPA analysis was carried out by first smoothing the RPA trace then taking the negative of the derivative of the collector current with respect to the ion retarding grid bias voltage. The result, plotted against the bias voltage, is proportional to the ion energy per charge distribution function.[16] The average ion energy per charge was calculated by averaging only the part of the trace where the amplitude exceeded half of the maximum amplitude. This averaging approach will be referred to as the threshold-based averaging approach with a 50% threshold. Figure 4 shows an example of applying the threshold-based averaging approach to an RPA trace. The black dashed vertical line indicates the location of the most probable voltage, the red solid vertical line indicates the result of using the threshold-based averaging approach with the 50% threshold, and the red dashed horizontal line indicates the 50% of maximum threshold.

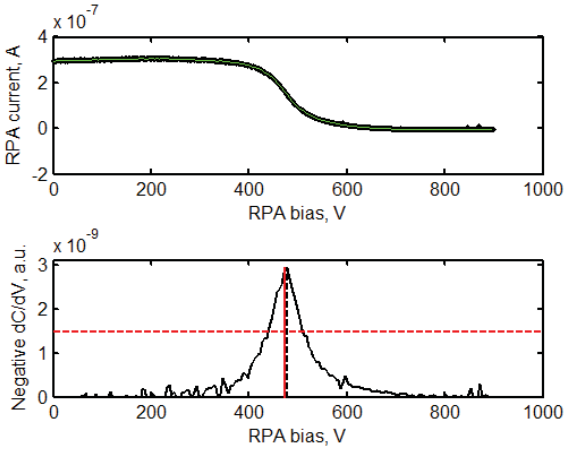

Figure 4. Sample RPA analysis plots.

In theory, the most accurate result is obtained by ensemble-averaging the entire RPA trace. However, doing so often produces unphysical results because the ion energy per charge distribution as measured by the RPA is typically much broader than the real distribution due to the wide acceptance angle of the RPA. Using the 50% threshold-based averaging approach strikes a balance between excluding the broadened data and maintaining noise insensitivity.

B. ExB Probe Analysis

The ExB probe is used as a velocity filter for charged species spectrometry. Since different charged species are accelerated to different velocities by going through roughly the same potential drop, they will show up as different peaks when interrogated by the ExB probe. For a scenario where the ExB probe velocity resolution is at least several times smaller than the width of the ion velocity distribution function (VDF), the preferred method for analyzing ExB probe data is via integration. Since the ion velocity distribution function (VDF) from different charged species tend to overlap in the regions between peaks, a direct integration of only one species at a time is impossible without assuming a VDF form. Furthermore, the domain of the curve-fit for each species typically needs to be bounded so that only the current signal generated by one species is being fitted at a time. Once the VDF form and the domain boundaries are chosen, the ExB probe data can be integrated for current and species fractions.

The integration formulas used for the present study differ from traditionally published formulas. More information regarding derivation of the new integration formulas and differences with the traditional formulas can be found in Huang's paper.[17]

For the present study, the form of the VDF was chosen to be skew-normal.[18] The mathematical form of the skew-normal distribution is shown in Eq. (8).

$$\text{Skew-Normal:} \quad f_j(u) = a * \exp\left[-\frac{(u-c)^2}{2b^2}\right] * \left\{1 + \text{erf}\left[-\frac{d*(u-c)}{\sqrt{2b^2}}\right]\right\} \tag{8}$$

Where a, b, c, and d, are fitting constants, and the term erf[] refers to the error function. Compared to a normal distribution, the skew-normal distribution has an additional parameter that controls skewness and collapses into a normal distribution when that parameter is equal to 0. The skew-normal distribution retains the general shape of the normal distribution but has skewness. Note the Gaussian distribution is essentially a normal distribution.

The skew-normal VDF form is inserted into Eq. (9)

$$I_{P,j}(V_P) = K_1 n_j V_P{}^3 f_j\left(\frac{V_P}{B_0 D_f}\right) \sim V_P{}^3 f_j(V_P) \tag{9}$$

Where $I_{P,j}$ is the contribution of the j-th species to the ExB probe collector current, n_j is the number density of the j-th species, V_P is the ExB probe bias, B_0 is the magnetic field magnitude in the ExB filter section, and D_f is the gap between ExB bias plates. K_1 is a constant. In practice, K_1, n_j, B_0, and D_f are constant with respect to the bias voltage and can be rolled into the fitting constants of the VDF forms. Curve-fits are then performed using Eq. (9) for each charged species in the ExB probe data in order to obtain the values of the various fitting constants.

For this study, the curve-fit process starts with the singly-charged species peak. The fitted curve is then subtracted out of the data and the remainder is curve-fitted for the doubly-charged species peak. The process is repeated until the quadruply-charged species peak is fitted. Boundaries are used to make sure the curve-fit is performed over domains that are dominated by only one charged species at a time. For each species, the left boundary is set to 0.9 times the voltage location of the corresponding species peak; the right boundary is set to halfway between the peak location of this species and the peak location of the next higher charged species. These values were found to work well for the fairly narrow VDFs found in the present study.

The voltage location of the singly-charged species is located via an automated algorithm. The ratio of the locations of the remaining peaks to the location of the singly-charged peak is assumed to be constant and found by manually studying several ExB probe traces. Visual inspection of the curve-fit process shows the code accurately locates the peak locations.

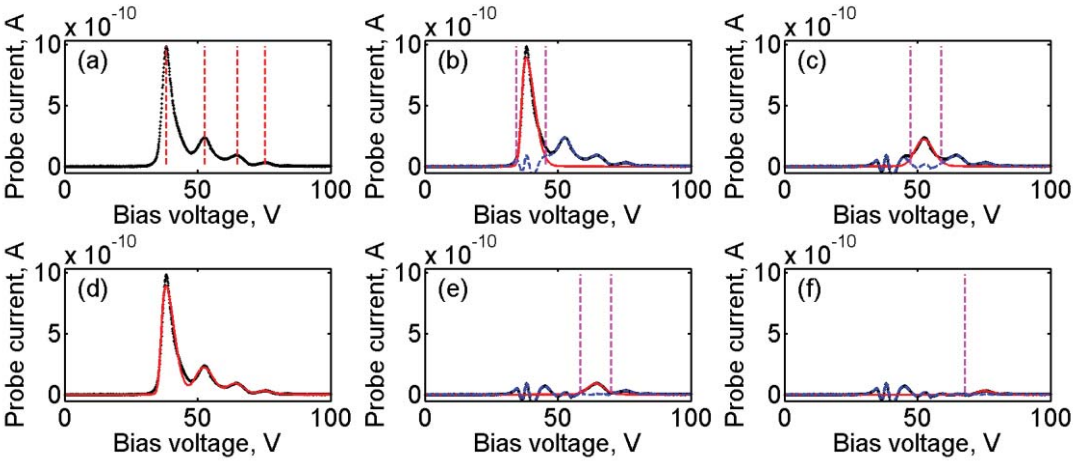

Figure 5. ExB probe analysis plots for the NASA HiVHAc EDU2 operating at 500-3.9-P1x.

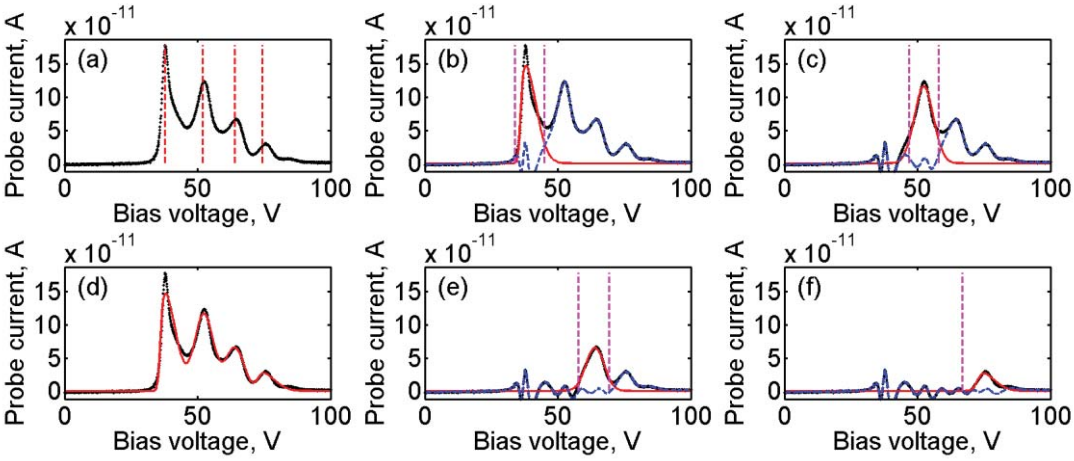

Figure 6. ExB probe analysis plots for the NASA HiVHAc EDU2 operating at 500-3.9-P5x.

Figures 5 and 6 show the analysis plots generated by the program that performs the ExB probe analysis for the 500-3.9-P1x and 500-3.9-P5x operating conditions. As a reminder, the labels indicate both plots correspond to the 500 V, 3.9 kW throttle point. The P5x case corresponds to a background pressure that is 5 times that of the P1x case as indicated by ion gauge 2. For convenience, the paper will refer to the six subplots in order from left to right, top to bottom as (a) to (f). Subplot (a) shows the raw ExB probe data as black data points with red dashed vertical lines showing the location of the first four peaks. Subplots (b), (c), (e), and (f) show the four sub-steps in the curve-fitting process. The program fits the appropriate equation to the 1st peak, subtracts the fitted data, then fits the 2nd peak, and so on. The data prior to the fit at each curve-fit sub-step are shown as black dots, the red solid line shows the curve-fit, the magenta dashed vertical lines show the curve-fit boundaries, and the blue dashed line shows the leftover result after subtraction. Subplot (d) shows the raw data in black dots with a red solid line that represents the sum of all four curve-fit sub-steps super-imposed on top.

Once the fitting constants were found, species fractions and current fractions could be calculated via Eqs. (10) and (11), respectively.

$$\zeta_j \equiv \frac{n_j}{\sum_k n_k} = \frac{\int_0^\infty \frac{I_{P,j}(V_P)}{V_P{}^3} dV_P}{\sum_k \int_0^\infty \frac{I_{P,k}(V_P)}{V_P{}^3} dV_P} \tag{10}$$

$$\Omega_j \equiv \frac{I_j}{\sum_k I_k} = \frac{Z_j \int_0^\infty \frac{I_{P,j}(V_P)}{V_P{}^2} dV_P}{\sum_k Z_k \int_0^\infty \frac{I_{P,k}(V_P)}{V_P{}^2} dV_P} \tag{11}$$

Where I_j is the current contributed by the j-th species at the entrance of the ExB probe collimator. Since the entrance orifice area is a constant across all I_j's, I_j and I_k can be replaced with the corresponding current densities. Note that I_j is not the same as $I_{P,j}$, which is current at the collector of the ExB probe. In this study, Xe^{4+} was not accounted for in the current and species fraction calculation because that population typically comprise less than 0.5% of the beam current.

To complete the analysis, CEX interactions between beam ions and facility background neutrals needed to be taken into account. CEX depletes lower-charge-state species more than higher-charge-state species, causing the ExB probe to read larger higher-charge-state species fractions than when in the vacuum of space. This effect is especially prominent for high-power thruster tests. The CEX model used to correct the ExB probe data is described in Shastry's work[5]. The model describes the effect of CEX as a set of attenuation factors that diminishes the detected current at the ExB collector. Eqs. (12)-(14) show the equations used to calculate the attenuation factors.[5]

$$(J/J_0)_{Xe^+} = \exp(-n_0\sigma_1 z), \quad \sigma_1 = 87.3 - 13.6\ \log(V_1) \tag{12}$$

$$(J/J_0)_{Xe^{2+}} = \exp(-n_0\sigma_2 z), \quad \sigma_2 = 45.7 - 8.9\ \log(2V_2) \tag{13}$$

$$(J/J_0)_{Xe^{3+}} = \exp(-n_0\sigma_3 z), \quad \sigma_3 = 16.9 - 3.0\ \log(3V_3) \tag{14}$$

Where J is the recorded current density at distance z away from the thruster exit plane, J_0 is the current density that would have been recorded at the thruster exit plane, and n_0 is the average background neutral density. The numerical formulas for the CEX cross-sections, σ_1, σ_2, and σ_3, are given in units of Å^2 (10^{-20} m^2). The ion energy per charge, V_1, V_2, and V_3 for Xe^+, Xe^{2+}, and Xe^{3+}, respectively, are assumed to be equal to the average ion energy per charge as measured by the RPA. The value of n_0 is calculated by converting the average of the pressure measurement from two ion gauges. One gauge is ion gauge 2 on the thrust stand and the other is the ion gauge on the facility wall. Note that one can assume the ion energy per charge is equal to the discharge voltage for the purpose of these calculations. Doing so removes the dependence of the ExB probe analysis on the RPA, though with a small increase in uncertainty. See Shastry's work for an estimate of this uncertainty.[5]

C. Faraday Probe Analysis

Faraday probe data are used to calculate the plume divergence angle and the total ion beam current. The cosine of the momentum-weighted plume divergence angle is defined as the average axial velocity of the particles divided by the average total velocity of the particles. However, momentum-weighted divergence angle is difficult to measure. The typical approach is to measure the charge-weighted divergence angle, which is approximately equal to the momentum-weighted divergence angle if the multiply-charged current fractions are roughly constant across the interrogated domain. For a polarly-swept probe, Eq. (15) can be used to calculate the charge-weighted divergence angle.

$$<\cos\ \delta> = \frac{2\pi R_{FP}{}^2 \int_0^{\pi/2} j(\theta)\ \cos\theta \sin\theta\, d\theta}{2\pi R_{FP}{}^2 \int_0^{\pi/2} j(\theta)\ \sin\theta\, d\theta} \tag{15}$$

Where δ is the charged-weighted divergence angle, θ is the polar angle and is equal to 0° for particles traveling parallel to the firing axis, and $j(\theta)$ is the ion current density as a function of the polar angle. R_{FP} is the distance from the Faraday probe collector to the thruster center at the exit plane and is constant for a polarly-swept probe. The denominator is equal to the total ion beam current.

For a nude Faraday probe with a guard ring like the one used in this study, the effective collection area is not exactly equal to the collector frontal surface area. Current that enters the gap between the collector and the guard

ring can be collected by the side surfaces of the collector.[19] According to work by Brown, the current entering the gap is collected by the collector and the guard ring in a ratio proportional to the ratio of exposed gap area.[19] For the probe design used in the present study, the area inside the gap is dominated by guard ring surfaces (see Fig. 3). However there is enough area connected to the collector that some level of correction is needed. Note that only the part of the gap with direct exposure to the incoming ion beam is used in the gap area calculation. Using the approach recommended by Brown, the effective collection area is ~4% greater than the collector frontal area. The effective collection area is used for all Faraday probe analysis.

Much like in ExB probe data analysis, CEX is a factor in Faraday probe data analysis. This study will follow many of the recommendations made in Brown's paper.[19] By taking Faraday probe data at multiple distances, the data can be used to extrapolate back to the thruster exit and should eliminate most of the facility-related CEX effect. Specifically, Eq. (15) is applied to the Faraday probe data from each of the four probe distances. The resulting value of $\langle \cos \delta \rangle$ are plotted against the distance from the thruster, and a second-order polynomial is used to extrapolate the value of $\langle \cos \delta \rangle$ at the thruster exit. This is identical to Brown's approach.

To calculate the total beam current at the thruster exit, the beam current is integrated for each of the four probe data sets and plotted against the distance from the thruster. A linear trend is fitted and extrapolated to the thruster exit. There has been little prior research on the correct form of the trend line and a linear fit was selected for simplicity.

Although the Faraday probe material chosen for this test, molybdenum, is considered a low SEE yield material, some correction for SEE effect is still needed. Secondary electrons born on a negatively biased probe will accelerate away from the probe. This effect adds extra current to the probe measurement that is indistinguishable from the collected ion current. While singly-charged xenon-induced SEE yield for molybdenum is very low, 0.022, the doubly-charged xenon-induced SEE yield is roughly 10 times that of the singly-charged yield, and the triply-charged SEE yield is roughly 35 times that of the singly-charged yield.[20-22] Furthermore, Hagstrum discovered that metastable singly-charged xenon induces roughly the same SEE yield as doubly-charged xenon.[23] Since the amount of multiply-charged species in the plume of a Hall thruster is typically not negligible, correction for SEE effect is needed.

Data published by Hagstrum will be used to correct for the effect of SEE on the Faraday probe measurement. Table 1 summarizes the SEE yield values used in the data analysis of the present study. The singly-charged and doubly-charged xenon-induced yields are averages of the SEE yield data for ion energies in the range of 200 to 800 eV in Hagstrum's 1956 work on molybdenum.[21] For both of these parameters, the value measured by Hagstrum varied by no more than 10% of the listed average. A published value for the triply-charged xenon-induced yield of molybdenum could not be found. The value in Table 1 is a projected value based on the similarity in yield between tungsten and molybdenum. The ratio of triply-charged induced yield to doubly-charged induced yield for tungsten is 3.5, so the yield for molybdenum is projected to be 3.5 * 0.2, or 0.7.

Table 1. Summary of SEE data for xenon ion bombardment of molybdenum.[20, 21]

Bombarding particle	SEE yield of molybdenum
Xe^{+}	0.022
Xe^{2+}	0.20
Xe^{3+}	0.70

Equation (16) shows the relationship between the actual ion current density and the ion current density measured by the Faraday probe due to SEE effect.

$$\frac{J}{J_{FP}} = \frac{1}{1 + \sum_{k} \frac{\Omega_k \gamma_k}{Z_k}} \tag{16}$$

Where J is the true ion current density, J_{FP} is the current density measured by a nude Faraday probe, and γ_k is the SEE yield in number of electrons per ion associated with bombardment by the k-th species. For the present study, the ion current density measured by the nude Faraday probe is 3 to 12% higher than the actual current density. The amount of metastable singly-charged ions is assumed to be negligible. This assumption is an extrapolation from controlled ion beam work done by Hagstrum.[23] In his experiment, Hagstrum varied the energy of the electrons used to generate his singly-charged ion beam from 10 to 70 eV. The SEE yield he measured jumped quickly up from 0.022 to 0.025 when the electron energy was ramped up from 25 to 30 eV, and then plateaued out at 0.025 all the way up to 70 eV. While the Hall thruster ionization zone and an ion beam discharge chamber are not exactly the same, they do share many of the same operating principles, including a reliance on impact bombardment ionization.

Since the amount of metastable ions was so small that the SEE yield increased by only 0.003 for Hagstrum's experiment, we assumed the effect will be of similar magnitude in a Hall thruster and is negligible.

D. Uncertainty Analysis

Uncertainty analysis will only be carried out for uncertainty elements that dominate the overall results. The uncertainty in the voltage utilization as calculated from Eq. (3) is ~1%. This uncertainty is a combination of the uncertainty in the RPA analysis method and the Langmuir probe analysis method used to correct the RPA measurement.

The uncertainty in the charge utilization as calculated from Eq. (7) is no more than 0.5%. This value is small because the charge utilization is very insensitive to the values of the current fractions.

ExB probe data is used to calculate the α_m term in the mass utilization. Based on the equations derived in Huang's paper,[17] the average velocity resolution of the ExB probe was 2.7%. This value is higher for ions with higher energy per charge and is no more than 4.0% for the detectable ion populations with the highest energy per charge. This resolution is sufficiently fine so that the aforementioned ExB probe analysis method is applicable. The ExB probe resolution primarily affected broadening of the measured VDF and has minimal effect on the current fractions. The uncertainty in the current fraction is expected to be dominated by the uncertainty in the average background neutral density measured by the ion gauges. The ion gauges are nominally 6% accurate. However, they only measured the neutral density in their immediate vicinity. Factors like conductance losses, electromagnetic radiation from the plasma, and un-compensated temperature effects on the electronics are expected to raise the uncertainty of the neutral density measurement to ~15%. Substituting in a ±15% neutral density uncertainty into the CEX correction formula yielded average uncertainties of ±0.040, ±0.022, and ±0.017 for the Xe^+, Xe^{2+}, and Xe^{3+} current fractions, respectively. The corresponding average uncertainty for α_m is 1.4%.

The Faraday probe data is used in the calculation of several efficiency factors, the uncertainties of each which will now be treated. For the divergence efficiency, the important sources of uncertainty include background CEX effects and SEE effects. As will be shown later in the results section, the Faraday probe may not have been working as intended during this study. Assuming it does work as intended, Brown's paper shows that the uncertainty is no more than 2% for the analysis method previously described.[19] The effect of SEE on the uncertainty of the divergence efficiency is more difficult to calculate due to lack of prior experience. However, as long as the current fraction only undergoes small changes as a function of polar angle, the overall effect will be small. This is because SEE represents a relatively small correction to the local current density; first-order changes to a first-order correction are second-order negligible. Thus, the overall uncertainty in the divergence efficiency is estimated to be 2%.

The uncertainty in the current utilization is primarily influenced by uncertainties associated with calculation of the effective collector area, CEX effects, and SEE effects. The effective collector area is expected to be accurate to ~1% based on different ways in which the gap current can be distributed between the collector and the guard ring. The use of the presented analysis method should produce results with uncertainty of no more than 2% based on prior work.[19] The uncertainty in the SEE calculation is tricky to estimate because it depends on the uncertainty of the current fractions calculated from the ExB probe data. Substituting in uncertainties in the current fractions previously calculated into the SEE correction equation (Eq. (16)), the uncertainty in the beam current due to SEE correction is 1%. The total uncertainty in the current utilization, calculated from standard error propagation, is 2.5%.

The uncertainty in the mass utilization is dominated by the uncertainty in the measured anode mass flow rate, the total beam current, and the current fraction-dependent factor, α_m. The mass flow rate measurement has an instrumentation uncertainty of ~1%. The uncertainty in the total beam current is the same as the uncertainty in the current utilization (2.5%). The uncertainty in α_m is 2%. The total uncertainty in the mass utilization, calculated from standard error propagation, is 3.4%.

V. Results

A. Langmuir Probe and RPA Results

Figure 7 shows the ion energy-per-charge distributions for the EDU2 thruster at the throttle point 500-3.9 with different background pressures. The distributions have been normalized by peak values. This figure illustrates a common trend seen in the RPA data; the distributions appear to become wider and average energy-per-charge drops slightly as the background pressure rises. The widening in the distribution is likely an artifact of the increasing amount of CEX reactions taking place in the farfield plume. The shift in peak energy-per-charge may indicate a real change in thruster physics.

Table 2 summarizes the results of the Langmuir probe and RPA analyses. This table shows the plasma potential with respect to facility ground from the Langmuir probe analysis, the average energy-per-charge from the RPA analysis with plasma potential correction, and the voltage utilization efficiency. Figure 8 shows the voltage utilization as a function of normalized background pressure. Table 2 and Figure 8 show more clearly the slight decrease in average energy-per-charge with rising background pressure. Since the value of energy-per-charge is calculated using the threshold-based averaging approach with a 50% threshold, it is largely immune to CEX effects, which tends to broaden the base of the energy-per-charge distribution that appears in an RPA trace.

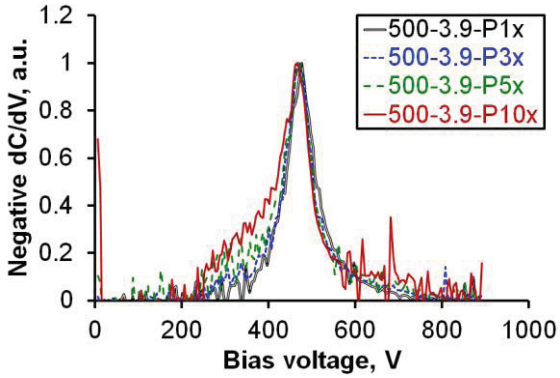

Figure 7. Ion energy-per-charge distributions for the throttle point 500-3.9 at different background pressures.

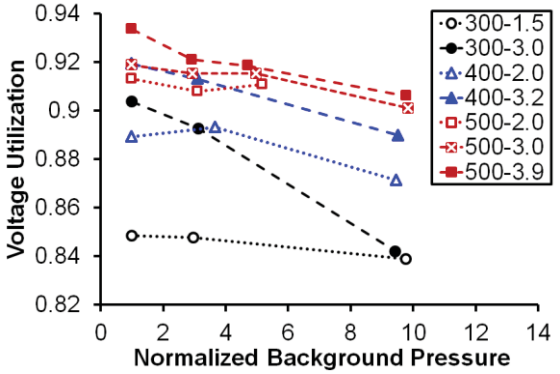

Figure 8. Voltage utilization efficiency as a function of normalized background pressure.

Table 2. Summary of voltage utilization efficiency analysis.

Disch. voltage, V	Disch. power, kW	Plasma potential, V				Energy per charge, V				Voltage utilization efficiency			
		1x	3x	5x	10x	1x	3x	5x	10x	1x	3x	5x	10x
300	1.5	7.2	7.2	-	6.9	255	255	-	252	0.848	0.848	-	0.839
300	3.0	5.3	6.6	-	6.3	271	268	-	253	0.904	0.893	-	0.842
400	2.0	8.1	7.8	-	6.6	356	357	-	349	0.889	0.893	-	0.871
400	3.2	6.9	7.2	-	7.8	368	365	-	356	0.919	0.913	-	0.890
500	2.0	5.9	6.9	6.5	-	457	454	455	-	0.913	0.908	0.911	-
500	3.0	7.5	7.5	7.2	7.2	459	458	458	451	0.919	0.915	0.915	0.901
500	3.9	6.9	8.4	7.5	6.9	468	461	460	454	0.934	0.921	0.919	0.906

B. ExB Probe Results

Figure 9 shows example ExB probe traces for the throttle point 500-3.9 at different background pressures. The traces have been normalized by peak values. This figure illustrates a common trend in the ExB probe data; the amount of multiply-charged species appears to grow with increasing background pressure. However, CEX attenuation will exaggerate the amplitude of multiply-charged species peaks, and the CEX effect increases with increasing background pressure. To study the trend further, data that has been corrected for CEX effect will be studied next.

Figure 10 shows the average charge state as a function of normalized background pressure for all tested throttling points. The average charge state is calculated using Eq. (17).

$$\bar{Z} = \sum_{k} Z_k \zeta_k \qquad (17)$$

The average charge state is an indicator of the amount of multiply-charged species present in the farfield plume.

Table 3 summarizes the results of the ExB probe analyses. The table shows the average charge state, α_m, and charge utilization efficiency. Figure 10 and Table 3 show that even after CEX attenuation is accounted for, there is a clear rise in the amount of multiply charged species as the background pressure rises. This rise appears to level off at high values of normalized pressure.

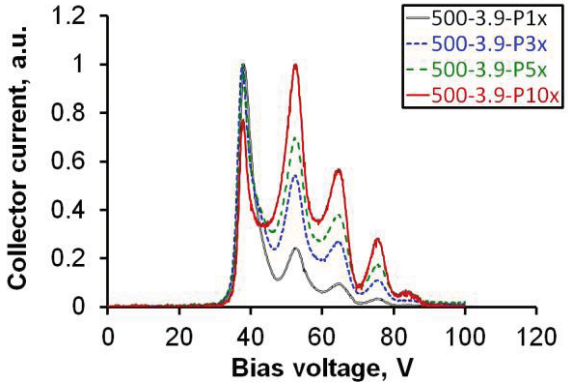

Figure 9. ExB probe traces for the throttle point 500-3.9 at different background pressures.

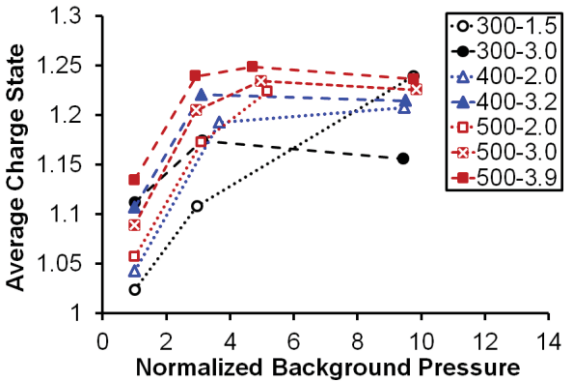

Figure 10. Average charge state as a function of normalized background pressure.

Table 3. Summary of charge utilization efficiency analysis.

Disch. voltage, V	Disch. power, kW	Average charge state				α_m				Charge utilization efficiency			
		1x	3x	5x	10x	1x	3x	5x	10x	1x	3x	5x	10x
300	1.5	1.024	1.108	-	1.239	0.968	0.870	-	0.759	0.994	0.978	-	0.962
300	3.0	1.112	1.174	-	1.156	0.866	0.809	-	0.828	0.976	0.967	-	0.970
400	2.0	1.043	1.193	-	1.207	0.943	0.790	-	0.780	0.989	0.964	-	0.963
400	3.2	1.107	1.221	-	1.215	0.872	0.773	-	0.780	0.977	0.964	-	0.965
500	2.0	1.057	1.172	1.224	-	0.925	0.809	0.769	-	0.986	0.968	0.963	-
500	3.0	1.089	1.205	1.234	1.226	0.890	0.784	0.764	0.772	0.980	0.965	0.963	0.964
500	3.9	1.134	1.239	1.248	1.236	0.846	0.761	0.755	0.766	0.974	0.963	0.962	0.964

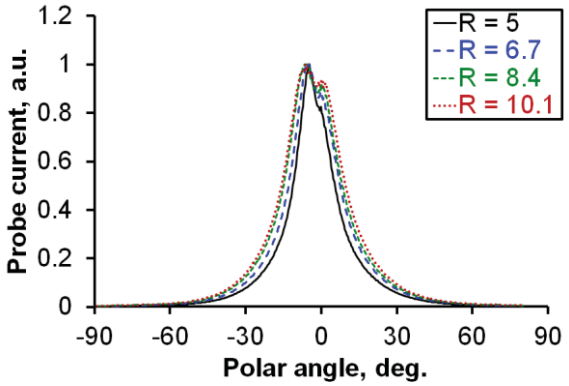

Figure 11. Faraday probe traces at different probe distances for the operating condition 500-3.9-P1x.

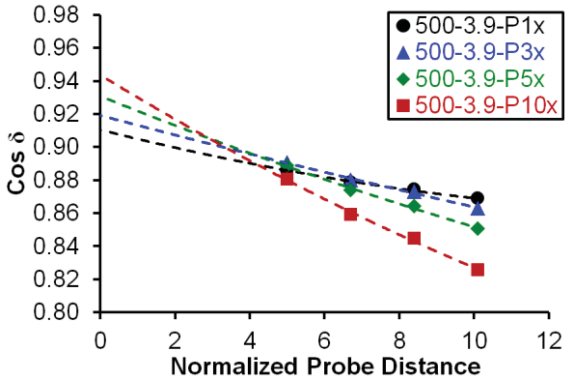

Figure 12. Cos δ as a function of normalized probe distance for the throttling point 500-3.9.

C. Faraday Probe Results and Comparisons

Figure 11 shows examples of Faraday-probe traces for the operating condition 500-3.9-P1x at different probe distances. All traces are normalized by peak probe current to better illustrate the change in width of the traces. This figure shows that the width of the Faraday probe trace increases with probe distance. This increase in width is due to the tendency of the CEX effect to redistribute ions from the center of the trace toward the edge of the trace.

Figure 12 shows extrapolation of the value of cos δ to the thruster exit for the throttle point 500-3.9 at different background pressures. Figure 13 shows the divergence efficiency as a function of normalized background pressure. The two figures show that the divergence of the plume appears to decrease with increasing background pressure.

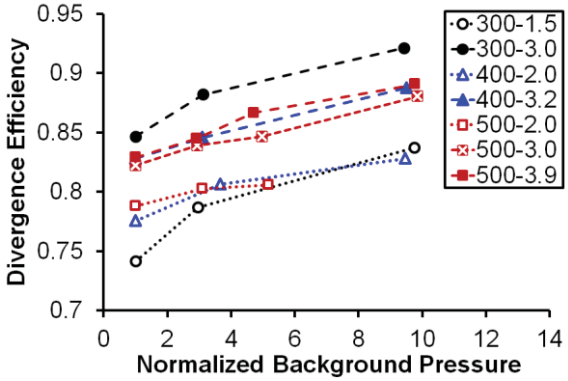

Figure 13. Divergence efficiency as a function of normalized background pressure.

Table 4 summarizes the results of the Faraday probe analyses for plume divergence. The degree of decrease in plume divergence appears to vary with the discharge voltage. For the 300 V throttling points, the decrease in divergence with a 10x rise in background pressure is ~7° while for the other throttling points, the decrease in divergence is 4-5°.

Table 4. Summary of divergence efficiency analysis.

Disch. voltage, V	Disch. power, kW	Divergence angle				Divergence efficiency			
		1x	3x	5x	10x	1x	3x	5x	10x
300	1.5	30.6	27.5	-	23.8	0.741	0.787	-	0.837
300	3.0	23.1	20.1	-	16.3	0.846	0.882	-	0.921
400	2.0	28.3	26.1	-	24.5	0.775	0.806	-	0.828
400	3.2	24.5	23.1	-	19.6	0.828	0.846	-	0.888
500	2.0	27.4	26.4	26.2	-	0.788	0.802	0.806	-
500	3.0	24.9	23.7	23.1	20.2	0.822	0.839	0.847	0.880
500	3.9	24.4	23.2	21.4	19.3	0.829	0.845	0.866	0.890

Table 5 summarizes the current utilization analysis. Table 6 lists the discharge current at various background pressures. Recall the anode mass flow is set to give the correct discharge power at the lowest achievable background pressure. The two tables show a rather surprising trend. The discharge current was increasing with background pressure while the beam current was decreasing. This strange trend will be explored in greater detail in the discussion section. Table 6 also lists the mass utilization efficiency, which depends strongly on both the ExB probe and the Faraday probe analyses. Two of the entries are slightly above unity, most likely due to measurement uncertainty. The decrease in measured beam current with rising background pressure appears to be the primary cause for the rapid drop in both the current and mass utilization with rising background pressure. Figures 14 and 15 show the current and mass utilization efficiencies as functions of normalized background pressure.

To conclude the efficiency analysis, Table 7 shows the thrust and the anode efficiencies calculated via thrust stand and probes. The effect of decreasing measured beam current becomes readily apparent in Table 7. At the highest background pressure setting (10x), the probe-derived anode efficiency is, on the average, 0.6 times that of the thrust-stand-derived anode efficiency. The standard deviation in the anode efficiencies is a fairly consistent percentage of the average and is small compared to the difference between the thrust-stand-derived and probe-derived values. We can conclude that the difference between thrust-stand-derived and probe-derived values is systematic. The combination of

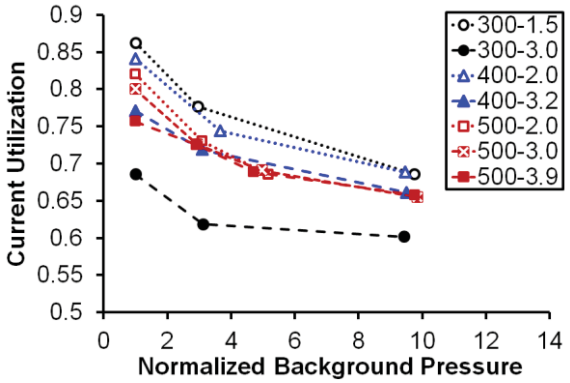

Figure 14. Current utilization efficiency as a function of normalized background pressure.

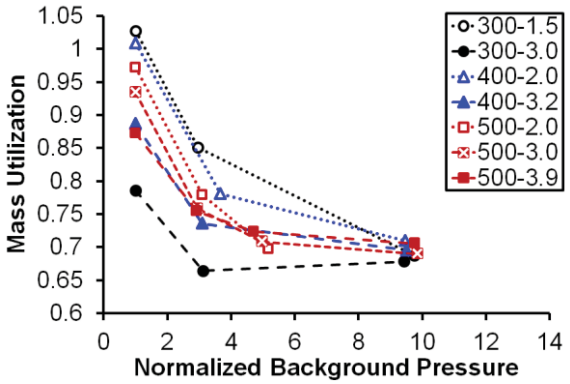

Figure 15. Mass utilization efficiency as a function of normalized background pressure

Table 5. Summary of current utilization analysis.

Disch. voltage, V	Disch. power, kW	SEE correction factor				Beam current, A				Current utilization efficiency			
		1x	3x	5x	10x	1x	3x	5x	10x	1x	3x	5x	10x
300	1.5	0.973	0.955	-	0.931	4.28	3.97	-	3.79	0.865	0.785	-	0.714
300	3.0	0.952	0.940	-	0.944	6.91	6.33	-	6.57	0.689	0.630	-	0.636
400	2.0	0.967	0.935	-	0.933	4.26	3.98	-	3.75	0.845	0.757	-	0.716
400	3.2	0.954	0.934	-	0.936	6.23	5.88	-	5.65	0.776	0.730	-	0.690
500	2.0	0.964	0.941	0.933	-	3.34	3.09	2.92	-	0.824	0.738	0.697	-
500	3.0	0.957	0.936	0.933	0.935	4.82	4.47	4.33	4.24	0.805	0.736	0.706	0.682
500	3.9	0.949	0.932	0.931	0.935	5.90	5.73	5.59	5.48	0.763	0.738	0.707	0.688

Table 6. Summary of discharge current and mass utilization analysis.

Disch. voltage, V	Disch. power, kW	Anode mass flow rate, mg/s	Discharge current, A				Mass utilization efficiency			
			1x	3x	5x	10x	1x	3x	5x	10x
300	1.5	5.47	4.95	5.06	-	5.31	1.030	0.859	-	0.715
300	3.0	10.31	10.03	10.06	-	10.32	0.790	0.676	-	0.718
400	2.0	5.39	5.04	5.26	-	5.24	1.013	0.794	-	0.738
400	3.2	8.27	8.02	8.05	-	8.19	0.893	0.747	-	0.725
500	2.0	4.31	2.03	2.09	2.09	-	0.976	0.788	0.709	-
500	3.0	6.21	2.99	3.04	3.06	3.12	0.940	0.769	0.724	0.718
500	3.9	7.73	3.88	3.89	3.96	3.99	0.880	0.767	0.743	0.738

Table 7. Summary of anode efficiency analysis.

Disch. voltage, V	Disch. power, kW	Thrust, mN				Anode efficiency from thrust stand				Anode efficiency from probes			
		1x	3x	5x	10x	1x	3x	5x	10x	1x	3x	5x	10x
300	1.5	85	90	-	95	0.443	0.487	-	0.521	0.557	0.440	-	0.345
300	3.0	188	191	-	196	0.568	0.587	-	0.599	0.407	0.324	-	0.343
400	2.0	105	109	-	110	0.505	0.521	-	0.539	0.583	0.417	-	0.367
400	3.2	172	175	-	181	0.555	0.575	-	0.602	0.516	0.406	-	0.381
500	2.0	92	95	96	-	0.481	0.498	0.510	-	0.570	0.410	0.349	-
500	3.0	139	144	146	149	0.520	0.547	0.559	0.577	0.560	0.419	0.382	0.375
500	3.9	182	186	188	194	0.549	0.573	0.580	0.602	0.506	0.424	0.402	0.395
Average:						0.517	0.541	0.550	0.564	0.528	0.406	0.378	0.365
Std. deviation:						0.045	0.040	0.036	0.040	0.061	0.038	0.027	0.020

the farfield probe data and the phenomenological model appear to still describe the physics of the thruster at 1x normalized background pressure but not at higher background pressures.

VI. Discussions

A. Two-Stream Ingestion Model

During the present study, we observed many of the same phenomena that had been observed in previous fixed-anode-mass-flow-rate studies; the thrust and discharge current both increase with background pressure.[24, 25] However, prior studies have performed limited engineering analysis on the effect of background pressure, engineering analysis that will be needed for further development work of the HiVHAc thruster.

To understand the implications of the results from the present study, a model of the background pressure effect is needed. In past studies, neutral gas ingestion is often cited as a possible explanation of the various observed thruster phenomena in high-background-pressure environments.[25, 26] A simplistic two-stream ingestion model is applied to the results from the present study. The two-stream ingestion model assumes the neutral flow in the thruster can be treated as two independent streams of neutrals superimposed on top of each other. One stream comes from the anode, ionizes in the ionization zone, and undergoes the full voltage drop measured by the RPA. The other stream comes from the background gas in the facility, ionizes somewhere in middle of the acceleration zone, and undergoes a voltage drop that should be a fraction of the full voltage drop. To simplify the model, the two streams are assumed to have the same propellant utilization, current utilization, and charge composition. Figure 16 illustrates the basic concepts of the two-stream ingestion model. Based on this model with the aforementioned assumptions, Eqs. (18), (19), and (20) can be written to describe changes in the thrust and discharge current as functions of background pressure.

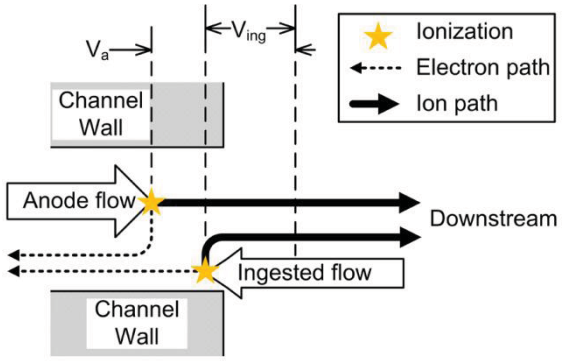

Figure 16. Illustration of the simplified two-stream ingestion model. *V_a and V_{ing} indicate voltages, not distances.*

$$T = \dot{m}_a \bar{u}_a + \dot{m}_{ing} \bar{u}_{ing} = \dot{m}_a K_1 \sqrt{V_a} + \dot{m}_{ing} K_1 \sqrt{V_{ing}}; \; K_1 \equiv \sqrt{\frac{2e\bar{Z}}{m_{Xe}}} \tag{18}$$

$$I_d = K_2 \left(\dot{m}_a + \dot{m}_{ing} \right); \; K_2 \equiv \left(\frac{\eta_m}{\eta_b} \right) \left(\frac{e}{m_{Xe}} \right) \left(\frac{1}{\alpha_m} \right) \tag{19}$$

$$\dot{m}_{ing} \equiv m_{Xe} A_{ing} w_{ing} n_{bg} \tag{20}$$

Where $\bar{u}_a$ is the average exhaust velocity of the anode stream, $\bar{u}_{ing}$ is the average exhaust velocity of the ingested stream, $\dot{m}_{ing}$ is the mass flow rate of the ingested stream, V_a is the acceleration potential for the anode stream,

approximated by the RPA measurement at the lowest background pressure, V_{ing} is the acceleration potential for the ingested stream, A_{ing} is the effective area over which ingestion is occurring, w_{ing} is the thermal speed of the background neutrals where the temperature is assumed to be room temperature (293 K), and n_{bg} is the neutral density calculated from the background pressure.

To find the various quantities in the model, the above equations will be manipulated. Since anode mass flow rate is fixed at a given throttling point for the present study, one can substitute Eq. (20) into Eq. (19) and define new constants to arrive at Eq. (21).

$$I_d = A_2 n_{bg} + B_2 \; ; \; A_2 \equiv K_2 m_{Xe} A_{ing} w_{ing} \; ; \; B_2 \equiv K_2 \dot{m}_a \tag{21}$$

Where A_2 and B_2 are constants that can be obtained by performing a linear curve-fit. Eq. (22) can then be used to calculate the effective ingestion area.

$$A_{ing} = \frac{A_2}{B_2} \frac{\dot{m}_a}{m_{Xe} w_{ing}} \tag{22}$$

The ingestion area can be used to calculate the ingestion mass flow rate. At this point, the thrust at 0 background pressure, or the vacuum thrust, can be obtained by plotting the thrust against either the background pressure or the ingested mass flow rate and extrapolating to 0. For this extrapolation, a linear fit was chosen. With both the ingestion mass flow rate and the vacuum thrust, one can use Eq. (18) to obtain the acceleration potential for the ingested stream. The $\dot{m}_a \bar{u}_a$ term is equal to the vacuum thrust.

Table 8 summarizes the application of the two-stream ingestion model to the HiVHAc EDU2 test data from the present study. Normalized ingestion area is the ingestion area divided by open area of the discharge channel. Ingestion percentage is defined as the ingested mass flow rate divided by the anode mass flow rate expressed in percentage. This table shows several very interesting trends. First, the area needed to account for the ingestion of background neutrals is a few times that of the open area of the discharge channel. This would make sense if ionization of the ingested stream is happening at or downstream of the exit plane, allowing more background neutrals than just those that enter the channel to participate. Second, the ingestion percentage is fairly small; 1-2% at 3x, 3-8% at 10x. Third, the acceleration potential of the ingested stream is well above the discharge voltage. This third trend implies that at least one of the simplifying assumptions of the model has broken down. A very likely culprit is that the charge composition of the plume changes noticeably with background pressure as seen in the ExB probe data.

At this point, there is enough information to determine the maximum allowable background pressure for accurate thrust measurements. Although the two-stream ingestion model incorrectly predicts the characteristics of the ingested stream, the associated equations yielded the slope of the curve-fit for thrust versus background pressure. Typical thrust measurements for a Hall thruster are ~2% accurate. To obtain accurate thrust measurements to within this uncertainty, the maximum allowable background pressure varies from 4×10^{-7} to 1×10^{-6} Torr. Moreover, if one uses these maximum background pressures with the model to calculate the ingestion rate, the maximum allowable ingestion percentage collapses to 1.2±0.2%. Thus, for future testing, a simple pre-test procedure to ensure accurate thrust measurements would be to measure thrust at several background pressures, and calculate the maximum acceptable background pressure. Alternately, for the HiVHAc EDU2, one can use the conservative background pressure to anode mass flow rate ratio, 5×10^{-7} Torr/(mg/s), to estimate the maximum acceptable background pressure.

Table 8. Summary of two-stream ingestion model results.

Disch. voltage, V	Disch. power, kW	Normalized ingestion area	Ingestion percentage				Ingested stream accel. potential, V		
			1x	3x	5x	10x	3x	5x	10x
300	1.5	4.0	0.8%	2.4%	-	7.9%	1477	-	578
300	3.0	2.2	0.3%	1.0%	-	3.4%	841	-	386
400	2.0	1.9	0.4%	1.4%	-	3.6%	2061	-	677
400	3.2	1.6	0.2%	0.7%	-	2.4%	3251	-	1798
500	2.0	3.6	0.9%	2.4%	4.1%	-	1311	843	-
500	3.0	2.1	0.4%	1.2%	2.1%	4.1%	2864	2366	1404
500	3.9	1.7	0.4%	1.0%	1.7%	3.3%	2600	2376	1583

B. Beyond Thrust Measurements

While the two-stream ingestion model produced some rough guidelines for determining the maximum acceptable background pressure for thrust measurements, it does not account for other types of testing, particularly life testing. A representative life test requires that the thruster not only generates a representative amount of thrust but is also operating in a manner comparable to on-orbit behavior.

The diagnostics used in the present study revealed some interesting changes in the physics of the HiVHAc EDU2 at high background pressure. For example, the average charge state appears to rise fairly quickly, then levels off with rising background pressure. At the same time, there is a gradual decrease in plume divergence and ion beam current with rising background pressure. The average energy per charge of the exhaust is seen to fall with rising pressure. Many of these trends cannot be explained by two independent mass flow streams. The far more likely scenario is that the ingestion of background neutrals is changing the physics of the thruster.

One possible explanation for some of the aforementioned trends is that the ionization and acceleration zones of the thruster are shifting upstream with rising background pressure. This phenomenon has been previously observed in Hall thrusters.[24, 27] If true, the plasma near the radial edges inside the channel would get cut off by the downstream corner of the channels leading to a decrease in the beam current density measured at high polar angles and a decrease in plume divergence, which matches result of the Faraday probe analysis. At the same time, the total beam current could drop as a result, although this could be countered by an increase in current from ingested ions.

The fall in average energy per charge of the exhaust could be explained by the two-stream ingestion model. The ingested stream should ionize further downstream than the anode stream and experience lower acceleration potential. Given the ingestion percentage reached up to 8% in the present study the magnitude of drop in average ion energy per charge measured by the RPA can be explained by ingestion.

The trend in average charge state cannot be explained by a simple model because it is non-linear. The sudden rise and leveling off in the relative amount of multiply-charged species suggest a change in physics. One explanation that was previous seen in literature is a change in plasma oscillation characteristics.[27, 28] For example, the dominant oscillation may have been one mode at 1x pressure but is another for 3x and higher. In such a case, the maximum acceptable pressure may have to be set to the point of transition. Both a high-speed camera and a set of high-speed Langmuir probes were used in the present study. The data will be processed next to study oscillation characteristics.

A final note regarding the plasma diagnostics used in this study, these analyzers and probes were not originally designed to operate in high-pressure environments. As such, the uncertainty in the probe data may be higher than calculated by the uncertainty analysis, which assumes a low-pressure environment. For example, an examination of the efficiency analysis shows that current and mass utilizations are much lower than what is typically seen in Hall thrusters suggesting that the Faraday probe was not properly capturing the entire ion beam current. There is a chance that some of the ions are being back-scattered out of the ±90° hemisphere. However, this effect is indistinguishable from a simple decrease in ion current. Additional studies are needed to determine whether the beam current truly decreased as much as reported herein.

VII. Conclusion

A plume characterization study with varying background pressure was performed on the HiVHAc EDU2 during the SSIT. The results indicated a rise in thrust and discharge current with background pressure. There was a decrease in average ion energy per charge, an increase in multiply-charged species production, a decrease in plume divergence, and a decrease in ion beam current with increasing background pressure.

A simplified two-stream ingestion model was applied. The results suggested that the effective ingestion area is a few times that of the open area of the discharge channel. Further analysis showed that the maximum acceptable ingestion percentage is around 1% for a thrust accuracy of 2%. The model was not able to predict a physical value for the acceleration potential of the ingested stream suggesting that this simple model is not sufficient for capturing certain characteristics of the plasma.

Examination of the plasma diagnostics results suggest the ionization and acceleration zones of the thruster were shifting upstream with increasing background pressure. There may also be a change in the operational characteristics of the thruster associated with the rapid change in average charge state. Future analysis on the high-speed data may shed light in this area.

Acknowledgments

We thank the NASA Science Mission Directorate In-Space Propulsion Technology project for funding this work. We thank Todd Peterson and Eric Pencil for managing this work. And we thank Kevin L. Blake and George P. Jacynycz for the thruster fabrication, assembly of the test setup, and operation of the vacuum facility.

References

[1]Dankanich, J. W., Kamhawi, H., and Mathers, A. J., "HiVHAC Maximum Operating Power Mission Impacts", *31st International Electric Propulsion Conference*, 2009-213, Ann Arbor, MI, 20-24 Sep., 2009.

[2]Kamhawi, H., et al., "Performance and Environmental Test Results of the High Voltage Hall Accelerator Engineering Development Unit", *48th AIAA/ASME/SAE/ASEE Joint Propulsion Conference & Exhibit*, AIAA-2012-3854, Atlanta, GA, 29 Jul.- 1 Aug., 2012.

[3]Huang, W., Kamhawi, H., and Shastry, R., "Farfield Ion Current Density Measurements before and after the NASA HiVHAc EDU2 Vibration Test", *48th AIAA/ASME/SAE/ASEE Joint Propulsion Conference & Exhibit*, AIAA-2012-4195, Atlanta, GA, 29 Jul.- 1 Aug., 2012.

[4]Kamhawi, H., Haag, T., and Huang, W., "Single String Integration of the High Voltage Hall Accelerator in NASA Glenn Vacuum Facility 5", *33rd International Electric Propulsion Conference*, 2013-445, Washington, DC, 6-10 Oct., 2013.

[5]Shastry, R., Hofer, R. R., Reid, B. M., and Gallimore, A. D., "Method for analyzing ExB probe spectra from Hall thruster plumes", *Review of Scientific Instruments*, Vol. 80, No. 6, doi:10.1063/1.3152218, 22 Jun., 2009, pp. 063502.

[6]Kim, V., "Main physical features and processes determining the performance of stationary plasma thrusters", *Journal of Propulsion and Power*, Vol. 14, No. 5, 1998, pp. 736-743.

[7]Hofer, R. R. and Gallimore, A. D., "High-Specific Impulse Hall Thrusters, Part 2: Efficiency Analysis", *Journal of Propulsion and Power*, Vol. 22, No. 4, doi:10.2514/1.15954, Jul.-Aug., 2006, pp. 732-740.

[8]Brown, D. L., "Investigation of Flow Discharge Voltage Hall Thruster Characteristics and Evaluation of Loss Mechanisms", Ph.D. Dissertation, Aerospace Engineering, University of Michigan, Ann Arbor, MI, 2009.

[9]Reid, B. M., "The Influence of Neutral Flow Rate in the Operation of Hall Thrusters", Ph.D. Dissertation, Aerospace Engineering, University of Michigan, Ann Arbor, MI, 2008.

[10]Pinero, L. R., Kamhawi, H., and Drummond, G., "Integration Testing of a Modular Discharge Supply for NASA's High Voltage Hall Accelerator Thruster", *31st International Electric Propulsion Conference*, 2009-275, Ann Arbor, MI, 20-24 Sep., 2009.

[11]Haag, T. W., "Thrust stand for high-power electric propulsion devices", *Review of Scientific Instruments*, Vol. 62, No. 5, doi:10.1063/1.1141998, May, 1991, pp. 1186.

[12]Kamhawi, H., Haag, T. W., Jacobson, D. T., and Manzella, D. H., "Performance Evaluation of the NASA-300M 20 kW Hall Effect Thruster", *47th AIAA/ASME/SAE/ASEE Joint Propulsion Conference & Exhibit*, AIAA-2011-5521, San Diego, CA, 31 Jul.- 3 Aug., 2011.

[13]Lieberman, M. A. and Lichtenberg, A. J., *Electrostatic Probe Diagnostics*, in *Principles of Plasma Discharges and Materials Processing*, 2nd ed., Ch., doi:10.1002/0471724254, Wiley, New York, 2005, pp. 185-203.

[14]Savitzky, A. and Golay, M. J. E., "Smoothing and Differentiation of Data by Simplified Least Squares Procedures", *Analytical Chemistry*, Vol. 36, No. 8, doi:10.1021/ac60214a047, Jul., 1964, pp. 1627-1639.

[15]Steinier, J., Termonia, Y., and Deltour, J., "Comments on Smoothing and Differentiation of Data by Simplified Least Squares Procedure", *Analytical Chemistry*, Vol. 44, No. 11, doi:10.1021/ac60319a045, Sep., 1972, pp. 1906-1909.

[16]Hutchinson, I. H., *Principles of Plasma Diagnostics*, 2nd ed., doi:10.1017/CBO9780511613630, Cambridge University Press, 2002.

[17]Huang, W., Shastry, R., Soulas, G. C., and Kamhawi, H., "Farfield Plume Measurement and Analysis on the NASA-300M and NASA-300MS", *33rd International Electric Propulsion Conference*, 2013-057, Washington, DC, 6-10 Oct., 2013.

[18]Azzalini, A., "A Class of distributions which Includes the Normal Ones", *Scandinavian Journal of Statistics*, Vol. 12, No. 2, 1985, pp. 171-178.

[19]Brown, D. L. and Gallimore, A. D., "Evaluation of Facility Effects on Ion Migration in a Hall Thruster Plume", *Journal of Propulsion and Power*, Vol. 27, No. 3, doi:10.2514/1.B34068, May-Jun, 2011, pp. 573-585.

[20]Hagstrum, H. D., "Auger Ejection of Electrons from Tungsten by Noble Gas Ions", *Physical Review*, Vol. 96, No. 2, doi:10.1103/PhysRev.96.325, 15 Oct., 1954, pp. 325-335.

[21]Hagstrum, H. D., "Auger Ejection of Electrons from Molybdenum by Noble Gas Ions", *Physical Review*, Vol. 104, No. 3, doi:10.1103/PhysRev.104.672, 1 Nov., 1956, pp. 672-683.

[22]Hagstrum, H. D., "Auger Ejection of Electrons from Tungsten by Noble Gas Ions", *Physical Review*, Vol. 104, No. 2, doi:10.1103/PhysRev.104.317, 15 Oct., 1956, pp. 317-318.

[23]Hagstrum, H. D., "Metastable Ions of the Noble Gases", *Physical Review*, Vol. 104, No. 2, doi:10.1103/PhysRev.104.309, Sep., 1956, pp. 309-316.

[24]Mazouffre, S., Pagnon, D., and Bonnet, J., "Two ways to evaluate the Xe^+ ion flow velocity in a Hall effect thruster", *40th AIAA/ASME/SAE/ASEE Joint Propulsion Conference*, AIAA-2004-3949, Fort Lauderdale, FL, 11-14 Jul., 2004.

[25]Walker, M. L. and Gallimore, A. D., "Performance Characteristics of a Cluster of 5-kW Laboratory Hall Thrusters", *Journal of Propulsion and Power*, Vol. 23, No. 1, doi:10.2514/1.19752, Jan-Feb, 2007, pp. 35-43.

[26]Randolph, T., et al., "Facility Effects on Stationary Plasma Thruster Testing", *23rd International Electric Propulsion Conference*, IEPC-1993-093, Seattle, WA, Sep., 1993.

[27]Nakles, M. R. and Hargus, W. A., Jr., "Background Pressure Effects on Ion Velocity Distribution Within a Medium-Power Hall Thruster", *Journal of Propulsion and Power*, Vol. 27, No. 4, doi:10.2514/1.48027, Jul-Aug, 2011, pp. 737-743.

[28]Diamant, K. D., Spektor, R., Beiting, E. J., Young, J. A., and Curtiss, T. J., "The Effects of Background Pressure on Hall Thruster Operation", *48th AIAA/ASME/SAE/ASEE Joint Propulsion Conference & Exhibit*, AIAA-2012-3735, Atlanta, GA, 29 Jul.- 1 Aug., 2012.